Chapter 55
Extreme Precipitation in the Himalayan Landslide Hotspot

Thomas Stanley, Dalia B. Kirschbaum, Salvatore Pascale, and Sarah Kapnick

Abstract Extreme precipitation from the South-Asian monsoon season combines with significant topographic relief within the Himalayan region to cause landslides that result in hundreds to thousands of fatalities each year. While there are few consistent and publicly available in-situ estimates of rainfall across this region, satellite products and global climate models provide insight into the extreme precipitation patterns that may impact the frequency of landsliding. In this work, we analyzed several extreme precipitation indices using data from a global climate model and the satellite-based Tropical Rainfall Measuring Mission Multi-satellite Precipitation Analysis product to represent extreme precipitation over High Mountain Asia. We then compared the temporal distribution of extreme precipitation to a global database of landslides to better understand the spatiotemporal distribution of potential landslide triggering factors. We found that these indices successfully model the seasonality of landslide activity across the region, but other aspects of spatiotemporal variability require additional information and analysis before they can be applied more broadly.

T. Stanley
Universities Space Research Association, Columbia, MD, USA

Goddard Earth Sciences Technology and Research, Greenbelt, MD, USA

Goddard Space Flight Center, NASA, Greenbelt, MD, USA
e-mail: Thomas.a.stanley@nasa.gov

D. B. Kirschbaum (✉)
Goddard Space Flight Center, NASA, Greenbelt, MD, USA
e-mail: dalia.b.kirschbaum@nasa.gov

S. Pascale
Department of Earth System Science, Stanford University, Stanford, CA, USA

S. Kapnick
Geophysical Fluid Dynamics Laboratory, NOAA, Princeton, NJ, USA

V. Levizzani et al. (eds.), *Satellite Precipitation Measurement*, Advances in Global Change Research 69, https://doi.org/10.1007/978-3-030-35798-6_31

Keywords Precipitation · Rainfall · Asian monsoon · Himalayas · TRMM · TMPA · Landslides · ETCCDI · Global climate models · NASA · GFDL FLOR · Global landslide catalog

55.1 Introduction

The Himalayan region is known as a landslide hotspot, with hundreds to thousands of associated fatalities each year (Nadim et al. 2006; Petley 2012). The pervasive distribution of landslides across this region is due to the combination of the world's greatest relief with heavy monsoon rainfall and occasional major earthquakes. While widespread landsliding can be triggered by a single earthquake or an earthquake with subsequent aftershocks (e.g., the 2014 Gorkha earthquake in Nepal), a large majority of landslides within this region, and around the world, are triggered by rainfall. Landslides within this region, which range from shallow debris flows to larger and more deep-seated failures, are typically triggered by short-duration, high-intensity monsoon rainfall (hours to days). One challenge in characterizing the spatiotemporal patterns in landslide activity within this region is the dearth of both landslide catalogs and in situ precipitation data that can be used to establish the co-occurrence, potential triggers, and even long-term trends in landslide activity. This work considers how satellite and modeled precipitation products can provide additional insight into the region's patterns of landslide activity, which are crucial when considering the global distribution of landslide risk.

Petley et al. (2007) observed an upward trend in the incidence of landslides that cause fatalities throughout Nepal from 1978 to 2005 and attributed this to development within rural development. However, the database from which this conclusion was drawn represents only a small portion of the total number of landslides. It is possible that trends in fatalities are more closely linked to changes in human exposure or vulnerability than trends in the occurrence of landslides in general. Given the difficulty of retrospectively reconstructing a multi-decadal record of landslide activity, gridded precipitation data offers an alternative view of the potential triggering mechanisms of landslide hazard with more consistency across time and space than hazard databases currently allow.

The investigation of extreme precipitation indices, and climate research in general, is justified in part by the belief that it provides information about the future of rainfall-triggered natural hazards, including landslides. The most commonly used extreme precipitation indices were formalized by an Expert Team on Climate Change Detection and Indices (ETCCDI) "to address the need for the objective measurement and characterization of climate variability and change" (World Climate Research Programme 2018). Unfortunately, the linkage between climate indices and landslide activity remains more of an assumption than comprehensively

illustrated. Cepeda et al. (2010) used R20mm (which records the number of days with very heavy precipitation) and other indices to corroborate trends from a susceptibility-based rainfall threshold. Chen et al. (2012) noted that 24-hour rainfall greater than 20 mm triggered numerous debris flows in the 5 years after the Chi-Chi earthquake. Statistically significant correlations have been observed between the indices Rx1day and Rx5day (maximum 1- or 5-day rainfall annually) and the annual number of landslides and flash floods reported in Rio de Janeiro, Brazil (Ávila et al. 2016). Similarly, Yang et al. (2016) correlated maximum streamflow with ETCCDI precipitation indices by month in the Huaihe Basin, China. Although the connection between extreme precipitation indices and landslide activity seems obvious, additional research is needed to establish a firm empirical relationship and examine the potential for generalization to other regions.

Warming trends in High Mountain Asia (HMA) climate are more clearly established than observed changes to extreme precipitation. A study of extreme precipitation in Nepal for the years 1970–2012 (overlapping Petley's landslide database, but longer by 15 years) revealed some trends, but the results were mixed (Karki et al. 2017). Likewise, observations of extreme precipitation in eastern and western zones of the Hindu Kush-Himalaya region showed contradictory and statistically insignificant trends from 1960 to 2000 (Panday et al. 2015). However, major increases in extreme precipitation, including 5-day precipitation, have been projected for both the eastern and western Himalayan zones by the end of the twenty-first century in multiple climate scenarios (Panday et al. 2015). The strong probability of increasing precipitation intensity over the next 80 years highlights the need to better understand how changes in extreme precipitation may impact landslide activity.

We have analyzed these indices with data from a global climate model (GCM) that was designed to better represent extreme precipitation in regional climates. For confirmation, we also prepared extreme precipitation indices from satellite observations. Next, we compared the temporal distribution of extreme precipitation to a global database of landslides. The results broadly confirmed the findings of previous research, but a large element of uncertainty regarding future patterns of natural hazards within the region remains.

55.2 Rainfall and Landslide Data

We derived the extreme precipitation indices from both GCM and satellite sources (Table 55.1). Numerical simulations were performed with the Geophysical Fluid Dynamics Laboratory Forecast-oriented Low Ocean Resolution version of CM2.5 (FLOR) (Vecchi et al. 2014). We also generated indices from the Tropical Rainfall Measuring Mission (TRMM) Multi-satellite Precipitation Analysis (TMPA; Huffman et al. 2010). In order to compare the changes in extreme precipitation to

Table 55.1 Data sources

Name	Temporal Coverage	Spatial Coverage	Grid Resolution (Degrees)	References
FLOR	2000–2016	Asia	0.625 × 0.5	Vecchi et al. (2014)
TMPA	1998-2019	50°N-50°S	0.25	Huffman et al. (2010)
GLC	2007–2016	World	Not applicable	Kirschbaum et al. (2015)

a record of landslide activity, we selected a portion of the Global Landslide Catalog (GLC), which provides information on rainfall-triggered landslides from 2007 to 2016 (Kirschbaum et al. 2015). The short time period for which the GLC was available limited a longer-term analysis of all three products (Table 55.1), so we performed other analyses for the joint time period of FLOR and TMPA.

55.2.1 GFDL FLOR

Numerical simulations are performed with the Geophysical Fluid Dynamics Laboratory Forecast-oriented Low Ocean Resolution version of CM2.5 (FLOR; Vecchi et al. 2014). FLOR has been derived from the GFDL Climate Model, version 2.5 (CM2.5; Delworth et al. 2011), which has been successfully used for studies of regional hydroclimatic variability and change (e.g., Delworth and Zeng 2014; Kapnick et al. 2014; Zhang et al. 2015; Delworth et al. 2016; Pascale et al. 2017). FLOR and CM2.5 are identical but differ in horizontal resolution in the ocean-sea ice components (~1 × 1°, with meridional resolution of 1/3° near the equator in FLOR, vs ~0.25° × 0.25°, with gridbox sizes ranging from 28 km at the equator to 8 km in polar regions in CM2.5).

In order to compare the FLOR output with observations over the period 2000–2016, simulated sea surface temperatures (SST) are nudged to the sea surface temperature monthly means observed during 2000–2016 by using the following SST tendency equation:

$$\partial SST(x,y,t)/\partial t = K(x,y,t) + \frac{1}{\tau}\left[SST(x,y,t)_T - SST(x,y,t)\right] \qquad (55.1)$$

where $\partial SST/\partial t$ is the time-tendency of sea surface temperature, K is the coupled model's tendency term worked out based on the model governing equations, and the last term on the right-hand side of the equation is the nudging (or restoring) term. This forces the modelled sea surface temperatures to relax, in timescale τ (the nudging timescale, 5 days) toward the target sea surface temperature SST_T, which in this case is the observed temperature. Because the ocean and the atmosphere are not initialized, the model's sea surface temperature would deviate from the

observed sea surface temperature without the last term in Eq. 55.1. Therefore, nudging allows the model to run forced by observed sea surface temperatures while still retaining atmosphere-ocean coupling at timescales shorter than 5 days. Similarly, surface pressure and three-dimensional temperature and horizontal winds are nudged every 6 hours towards reanalysis data. Full details are provided in Yang et al. (2018).

55.2.2 TMPA

The TMPA precipitation product provides estimated precipitation from 50°N-S from 1998 to the present. In this work, we used the research version of TMPA Version 7, which is available approximately 3 months after acquisition and is calibrated with the Global Precipitation Climatology Project (GPCP) gridded gauge dataset (Adler et al. 2003). TMPA was developed to utilize an international constellation of microwave and infrared satellite-borne instruments to produce 3-hourly estimates of total precipitation. There are known issues with satellite retrievals over complex terrain due to orographic uplift (Barros et al. 2000, 2004; Bharti and Singh 2015). However, in this study we considered the precipitation retrievals collectively across the entire study domain as well as at the pixel scale to represent potential bias that may occur when evaluating within smaller spatial domains influenced by orographic rainfall processes.

55.2.3 Landslide Data

The Global Landslide Catalog (GLC) provides a global picture of rainfall-triggered landslides based primarily on media reports. The database has over 11,000 entries and includes information on the location (geographic and nominal) and date, impacts, trigger, confidence in the location, qualitative estimate of the size, source of the report, etc. The catalog is known to have biases resulting from reporting sources that are primarily in English, uncertainty about the location and date, as well as issues differentiating landslides from other triggering hazards such as flooding and severe storms or tropical cyclones. The methodology for compiling this inventory and the characterization of the biases is available in Kirschbaum et al. (Kirschbaum et al. 2010, 2015). For this analysis we selected 1076 landslides within an analysis area that includes Nepal, northern India, and small portions of Pakistan and China where the largest proportion of the landslides have been reported (Fig. 55.1).

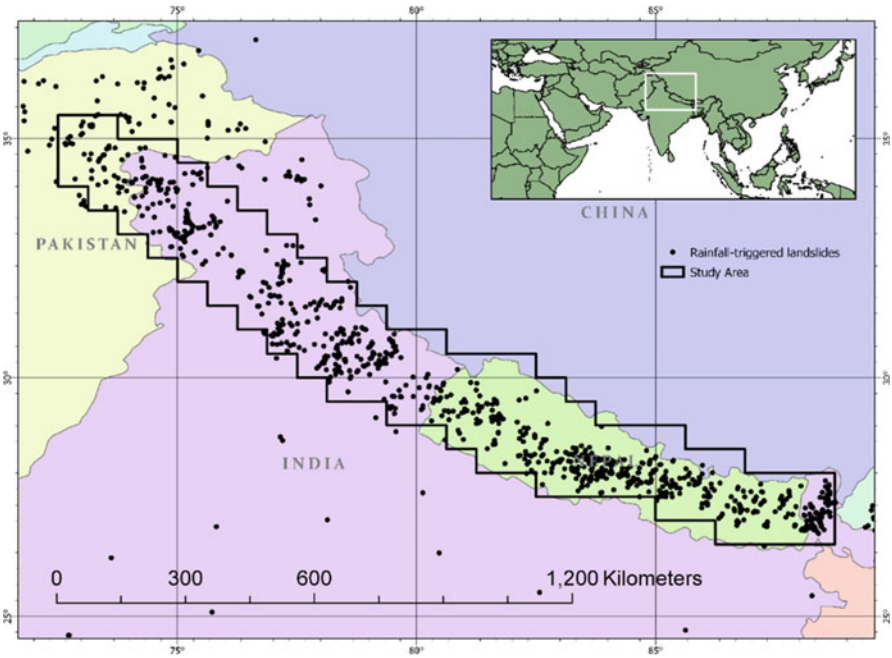

Fig. 55.1 The Global Landslide Catalog reveals a band of terrain with a high number of landslides (black dots indicate landslides from 2007–2016). The Himalayan Mountains and Foothills experience intense monsoon precipitation and occasional seismicity, while comprising some of the Earth's steepest terrain. We focused our analysis on this region by identifying the sites with the greatest elevation difference from neighboring pixels at the half-degree scale (black box). Unless otherwise noted, results are presented for this region

55.3 Methods

Landslides can be triggered by high-intensity, short-duration rainfall, as well as prolonged rain at lower intensities. We selected several of the extreme rainfall precipitation indices from the ETCCDI that are most likely to be relevant to landslide activity. We calculated Rx1day, Rx5day, R10mm, R20mm, CWD, R95pTOT, and R99pTOT (Table 55.2) from both FLOR (https://doi.org/10.5067/W8DR3VBR27PX, last accessed 5 Apr. 2019) and TMPA (https://doi.org/10.5067/5VPZ8AZ9LAKP, last accessed 5 Apr. 2019) products. Rx1day represents the most extreme daily precipitation, a level which is likely to generate landslides. Similarly, Rx5day represents the most extreme precipitation over a 5-day period, which is relevant to the landslides that may be caused by a gradual buildup of groundwater. R10mm and R20mm show the frequency of heavy precipitation, which represents the number of times that landslides are possible, if not guaranteed. Some landslides, especially deep-seated landslides, may be driven more by the duration than the intensity of rainfall. CWD addresses this possibility by showing the length of precipitation events. R95pTOT and R99pTOT represent the annual total amount of extreme precipitation. Because extreme

Table 55.2 Extreme precipitation indices selected for relevance to landslides

Index	Definition
Rx1day	The highest 1-day precipitation.
Rx5day	The highest sum of precipitation from 5 consecutive days.
R10mm	The number of days on which 10 mm or more of precipitation occurred.
R20mm	The number of days on which 20 mm or more of precipitation occurred.
CWD	The longest number of consecutive days with precipitation greater than 1 mm.
R95pTOT	The sum of precipitation on days that exceeded the 95th percentile precipitation, which is typically based on a historical period of 1961–1990. In this case, the base period was set to the 1999–2017 period for the TMPA data, because the earlier period is not available for this dataset.
R99pTOT	The sum of precipitation on days that exceeded the 99th percentile precipitation, which is typically based on a historical period of 1961–1990. In this case, the base period was set to the 1999–2017 period for the TMPA data, because the earlier period is not available for this dataset.

precipitation is defined against local historical conditions, these indices might be more closely associated with landslide activity than single, global thresholds. Although most of these indices can be calculated on a monthly basis, we focused on annual relationships. Monthly means were calculated for Rx1day and Rx5day in order to observe the seasonality of extreme precipitation. The geographic distribution of extreme precipitation was summarized for each index by taking the mean of annual values for the years 2000–2016. All indices were computed in R with the climdex.pcic library (R Core Team 2013; Bronaugh 2015; Hijmans 2015; Revolution Analytics and Weston 2015; Pohlert 2017).

We characterized the trend lines at each location for the precipitation indices based on the computed annual values using the Theil-Sen method for slope estimation (Sen 1968; Theil 1992), with statistical significance from the Mann-Kendall test (Mann 1945; Kendall 1948). These are commonly used in hydrology because nonparametric methods do not require an assumption of Gaussian residuals. The slope is defined as the median of the slopes derived from all possible pairs of data points. Thus, for ($1 \leq i < j \leq n$),

$$slope = median\left(\frac{x_j - x_i}{j - i}\right) \tag{55.2}$$

For this application, i and j represent years in the study period, and x represents the extreme precipitation index at a point. The Mann-Kendall test statistic is defined as:

$$S = \sum_{k}^{n-1} \sum_{j=k+1}^{n} sgn\left(x_j - x_k\right) \tag{55.3}$$

where j and k represent years in this dataset, and x represents the precipitation index at those times. These methods ensured that the volatility over the short time period represented by TMPA would be accounted for when identifying trends.

In order to understand the climate trends most relevant to landsliding, we focused on the region of High Mountain Asia with the highest concentration of landslides: the Himalayan foothills and mountains (Fig. 55.1). The analysis of precipitation extremes in FLOR is therefore restricted to only those grid-points with a slope threshold of 0.6 or larger. While somewhat arbitrary, this choice effectively selects a band of grid points along the zone of rapid elevation increase where most landslides take place. The area was used as a mask, which was then converted with the nearest-neighbor method to match the spatial resolution of TMPA. We applied the mask to all of the precipitation indices before comparing extreme precipitation to landslides. In order to evaluate differences between the eastern and western Himalaya, we divided the study area at 80°E (close to Nepal's westernmost point) into roughly equal parts. The number of landslides reported was also roughly equal (516 in the west and 560 in the east).

55.4 Results

55.4.1 Regional Patterns in Extreme Precipitation

We found very similar geographic distributions of extreme precipitation from FLOR and TMPA and broad similarities between the ETCCDI indices (Fig. 55.2). Indices that represent rainfall frequency more than intensity (CWD and R10) are highest at higher elevations, while indices that solely represent rainfall intensity (Rx1day and Rx5day) are generally higher at lower elevations near the boundary between mountains and plains. R20mm, R95pTOT, and R99pTOT are determined by both the frequency of intense precipitation and while generally related to the elevation have a less clear geographic relationship. In general, FLOR shows the heaviest precipitation at higher elevations than TMPA. The biggest difference between datasets is the high number of consecutive wet days observed in FLOR, more than double the number from TMPA (firm empirical connection 2a). This may be due to the well-known GCM "drizzle-bias", which is often handled using a minimum threshold (e.g., > 1 mm) so that the total number of wet days in the model and observations are equivalent (e.g., Ines and Hansen 2006). There may also be a bias in the opposite direction for TMPA since the passive microwave frequencies onboard TRMM's Microwave Imager (TMI) are not sensitive to light rain. Despite this sharp difference in magnitude, the spatial distribution of CWD is quite similar across datasets. In a few grid cells, mean annual Rx1day exceeds 144 mm, a landslide-triggering rainfall threshold derived empirically from rainfall gauge data across Nepal (Dahal and Hasegawa 2008).

The extreme precipitation indices calculated from TMPA precipitation show decreasing frequency and intensity of extreme precipitation in Nepal, but increases

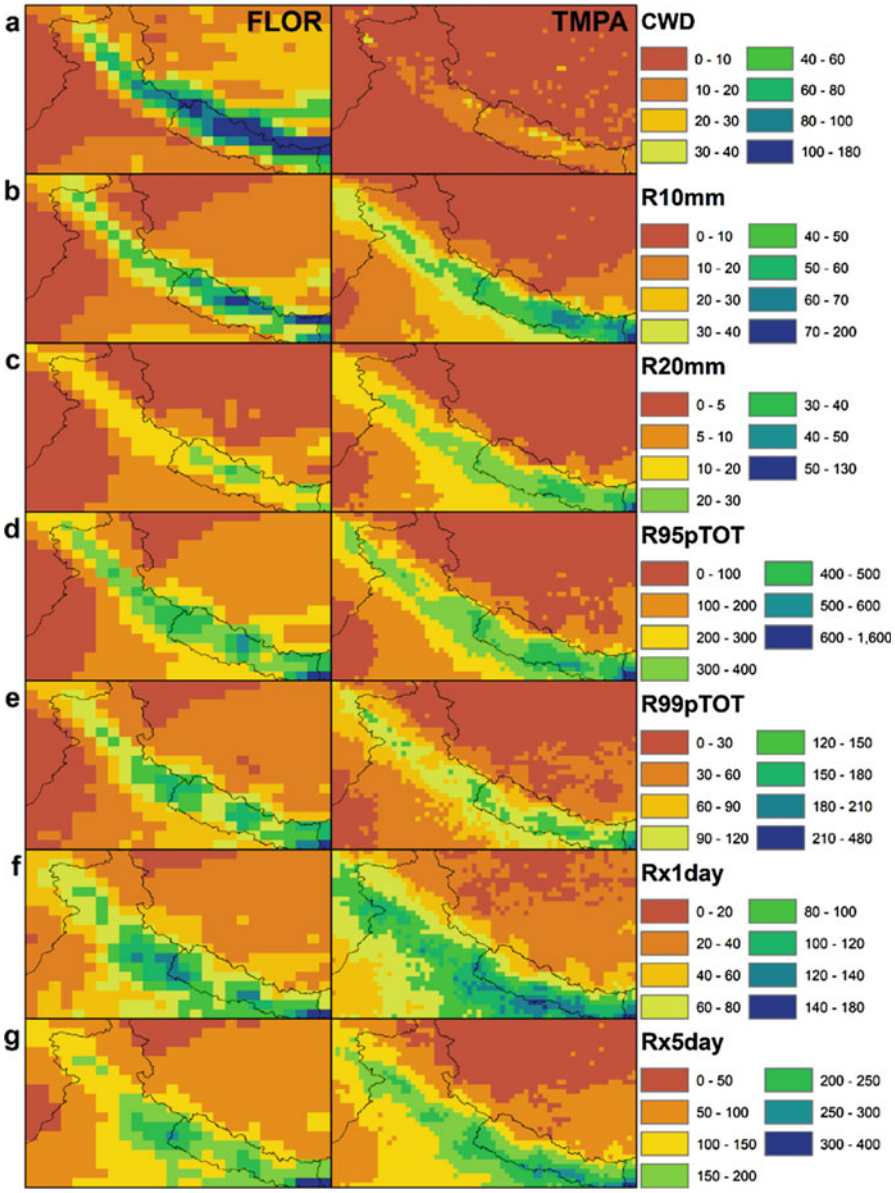

Fig. 55.2 Mean annual values of extreme precipitation indices: (**a**) CWD, (**b**) R10mm, (**c**) R20mm, (**d**) R95pTOT, (**e**) R99pTOT, (**f**) Rx1day, (**g**) Rx5day for GFDL FLOR (left) and TMPA (right). The data products show similar values and geographic distributions for all indices except CWD

in Kashmir, Rajasthan, and a section of Tibet (Fig. 55.3). CWD is the exception to the general trend in some places; it shows some decreases in Kashmir and some increases in southern Nepal. The indices derived from FLOR data show rough

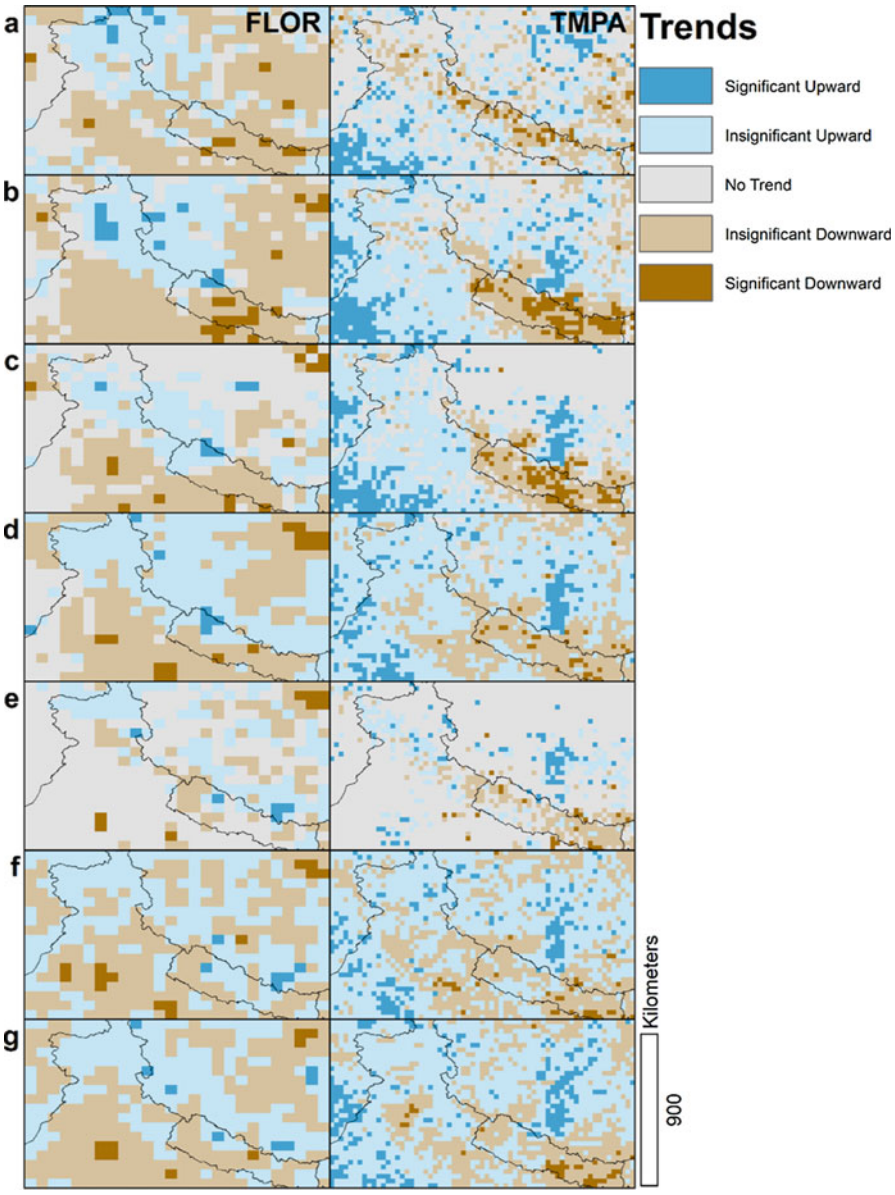

Fig. 55.3 Trends in extreme precipitation indices from 2000–2016: (**a**) CWD, (**b**) R10mm, (**c**) R20mm, (**d**) R95pTOT, (**e**) R99pTOT, (**f**) Rx1day, (**g**) Rx5day for FLOR (left) and TMPA (right)

geographic similarities to those from TMPA, but exhibit strong similarities with each other. In general, FLOR-based indices also show increases in Kashmir, but the trends in Nepal are less consistently negative. For both datasets, trends are not statistically significant in most locations, and the statistically significant trends are not consistently located in the same grid cells across indices and data products.

Although a gauge-based dataset for Nepal covers a much longer time period (Karki et al. 2017), similar trends were observed here. Analysis of R95pTOT, Rx1day, and Rx5day showed mixed but primarily decreasing trends for Central and Eastern Nepal at both meteorological stations and in the gridded products. Similarly, most of Nepal's precipitation gauges showed primarily decreasing trends in R10mm and R20mm, except in the high mountain region. Again, this largely matches the current results from the gridded datasets. CWD presented a mixed record across Nepal, and it is hard to summarize concisely the relationship between the datasets, but Karki et al. (2017) found that CWD was generally decreasing in southern Nepal and increasing in northern Nepal, while Fig. 55.3 shows the opposite pattern. Overall, the trends in extreme precipitation observed at Nepal's meteorological stations mirror the current results, despite the differences in methodology and time period.

55.4.2 Annual Variability

At the annual level, extreme precipitation indices appear to be poorly correlated with landslide activity (Fig. 55.4). In particular, 2007, 2008, 2009, and 2014 have very

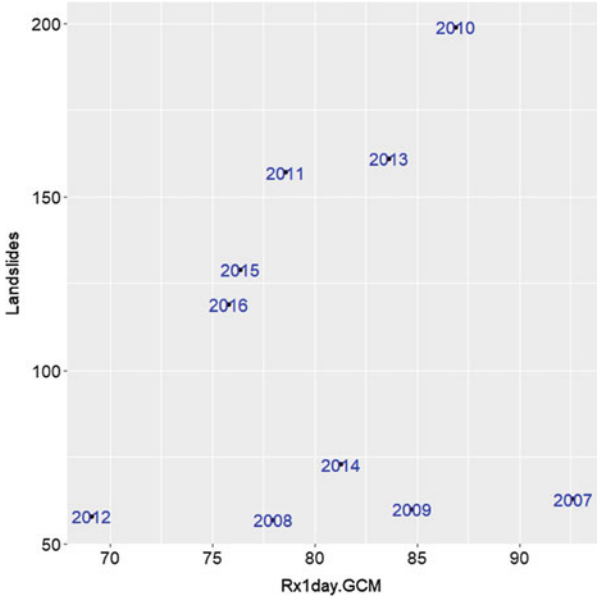

Fig. 55.4 Mean annual Rx1day (x-axis) from FLOR is not highly correlated with landslide activity from the GLC (y-axis). However, the first 3 years of the GLC (2007–2009) may have been underreported. If so, the relationship between extreme precipitation and landslide frequency might be strongly positive

few landslides compared to years with similar Rx1day values. However, the relationship between landslides and extreme precipitation would be fairly strong if evaluated after 2009. The other extreme precipitation indices show a similar pattern.

55.4.3 Seasonal Variability

The seasonal distribution of extreme precipitation in High Mountain Asia is dominated by the monsoon (June–September), although tropical cyclones may occasionally bring heavy rain or snow after the monsoon. As a result, rainfall-triggered landslides are also most abundant in South Asia at this time (Froude and Petley 2018). Landslide activity peaks in July, but is relatively high throughout the monsoon (Fig. 55.5). From October to May, fewer than 5 landslides per month are typically recorded in the GLC. This matches the cycle observed for both Rx1day and Rx5day. FLOR shows a peak of extreme precipitation in February, but this is not matched by a corresponding peak in landslide activity. TMPA also exhibits a peak but it is much less prominent. At the monthly scale, mean Rx5day derived from FLOR roughly doubles Rx1day, with relatively little variation (Fig. 55.6). The eight months with the highest mean value of Rx5day all coincide with the summer monsoon. Thus, both Rx1day and Rx5day encapsulate the seasonality of landslide activity.

Seasonality across the study region was also examined east and west of 80°E (Fig. 55.7). Although the monsoon dominates the seasonal climate cycle of both

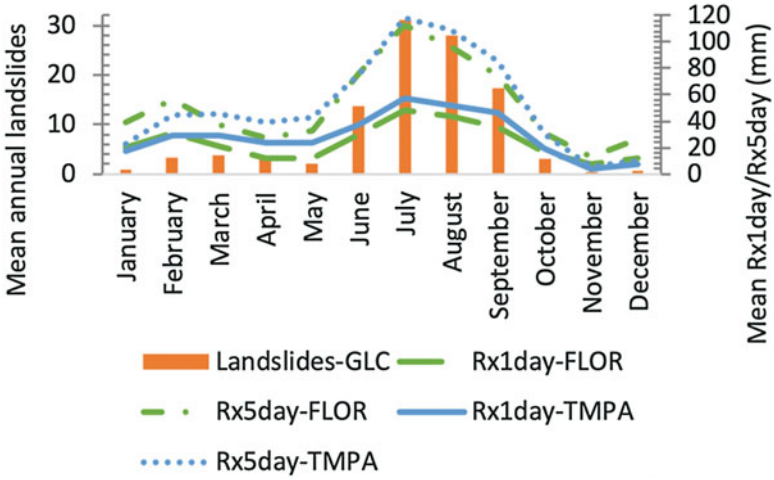

Fig. 55.5 The monthly pattern of landslide activity mirrors the extreme precipitation indices Rx1day (light colors) and Rx5day (dark colors). Landslide activity is represented by the total number of events recorded within the study area for each month from 2007 to 2016 in the GLC (orange). Daily precipitation was obtained from FLOR (green) and TMPA (blue)

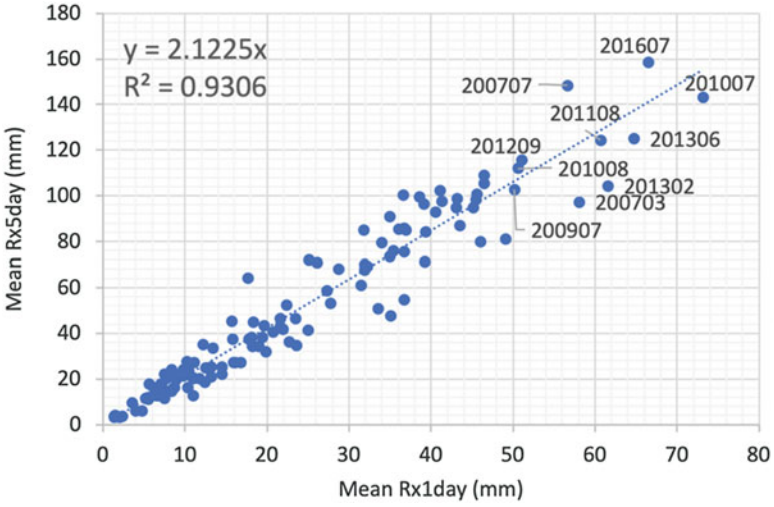

Fig. 55.6 The monthly means for Rx1day and Rx5day derived from FLOR are highly correlated. Precipitation is typically most intense during the monsoon, but February 2013 and March 2007 are exceptions

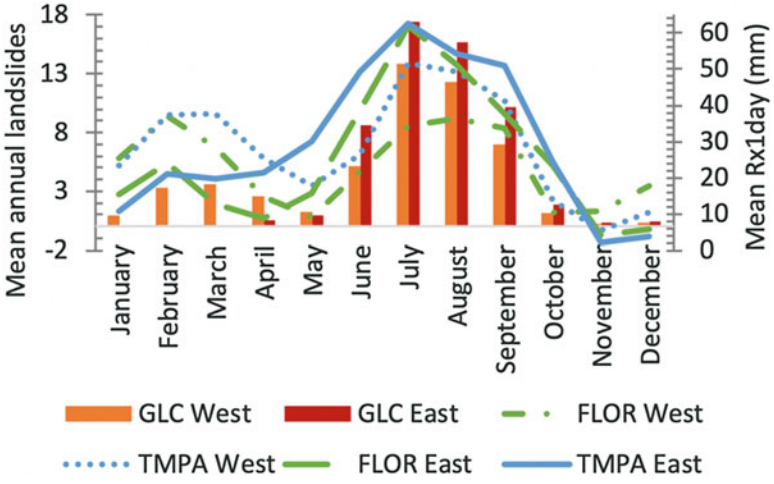

Fig. 55.7 The study area was divided into roughly equal halves at the 80th meridian, which left 516 (560) landslides in the western (eastern) section. The monthly distribution of landslides is similar, but the western portion of the study area experiences a secondary peak of landslide activity in March. Both FLOR and TMPA show a lesser peak in extreme precipitation during February, especially west of 80°

halves of the study area, the western region also experiences a smaller peak in landslide activity in March. Both regions experience high levels of landslide activity from June to September, with a peak in July. In general, this corresponds to the peak

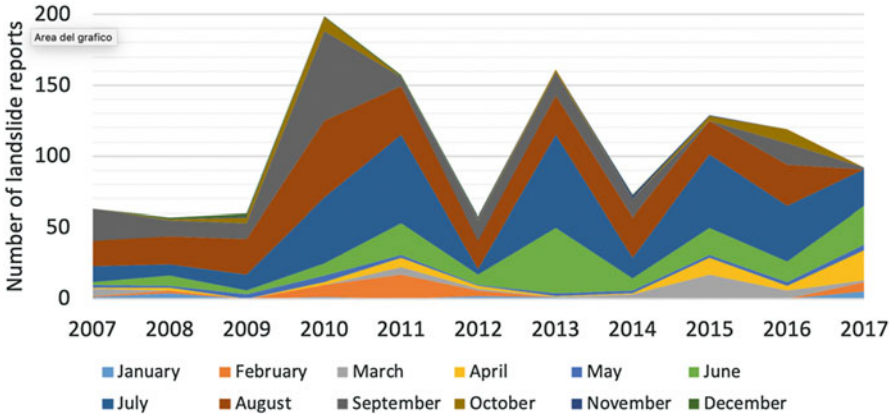

Fig. 55.8 Distribution of the GLC by month and year. June, July, August, and September dominate the record, but some years show little landslide activity in one or more of these months

in extreme precipitation. The exception is the western zone as estimated by FLOR, where the February peak in Rx1day slightly exceeds the monsoonal peak in August. In each region, less than 1 landslide is typically reported for the months of November, December, and January. Both FLOR and TMPA show a low in precipitation during November—nearly zero in the eastern half. This is followed by rising precipitation throughout the winter. This pattern of low landslide activity continues until June in the eastern portion of the study area (Fig. 55.7). On average, a few landslides are reported in the western zone during the months of February, March, and April. However, the mean value reflects a high level of inter-annual variability. 52% of the landslides reported in February occurred in 2011, and 46% of March landslides occurred in 2015 (Fig. 55.8). Rx1day also peaks in February (FLOR) and March (TMPA) over the western zone (Fig. 55.7). Although variable across the decade 2007–2016, the seasonality of extreme precipitation and landslide behavior was well reflected by Rx1day, whether averaged across the entire region or its eastern and western halves.

The total number of landslides reported in the GLC varies substantially, both by year and by month. As of this writing, the GLC has not been completed for 2017, so we have not included it in other analyses. Overall, annual variation is quite strong, with more than 3 times as many landslides in 2010 than in 2012. However, the number of reports is consistently low during the first three years of the GLC. July is the most active month on average, but fewer landslides are reported for July than for August or September 2007–2009, or for most years in the database. The wide range of landslide behavior can be explained, at least in part, by extreme precipitation.

The abnormally high number of landslides recorded in 2010 is explained by the 63 landslides that occurred across the region in September, more than the total number recorded for the years 2008, 2009, and 2012. In contrast, 2015 is notable for the total lack of landslides recorded in September and the record number of landslides in March. Landslides that occurred in 2017 had not been completely

catalogued at the time of writing, but the record thus far indicated a relatively active year, especially during the month of April.

55.4.4 Monthly Variability

We analyzed extreme precipitation by individual month to better understand the annual fluctuations in landslide activity. Mean Rx1day appears to have a nonlinear positive relationship with the monthly landslide total (Fig. 55.9). Monthly mean values below 15 mm are associated with very low levels of landslide activity. Above 15 mm, increasing Rx1day appears to generate increasing numbers of landslides, albeit with a high amount of variation. This is consistent with the existence of an intensity threshold below which landslides will rarely be triggered by rainfall (Gabet et al. 2004). More than 30 landslides occurred in nine months, all during the monsoon period. While the precipitation intensity was usually in proportion to number of landslides, the three months with more than 60 landslides (September 2010, July 2011, and July 2013) actually had mean Rx1day less than 40 mm. This is a high number, but not relative to many other months. Another group of outliers can

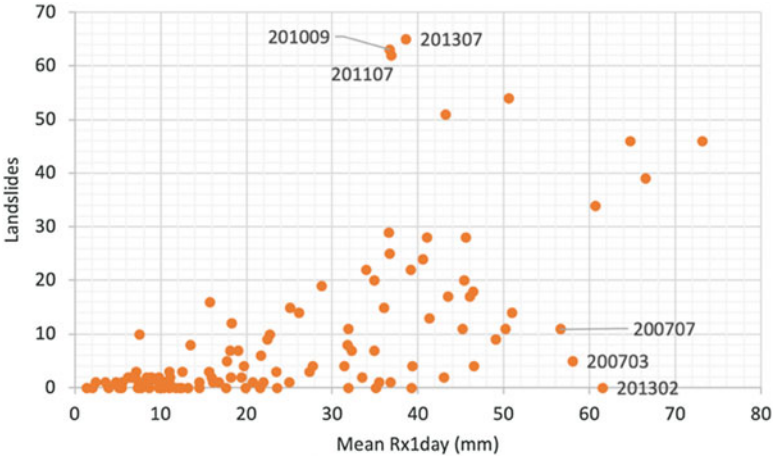

Fig. 55.9 FLOR monthly mean values of Rx1day are weakly correlated to the monthly number of landslides reported in the GLC. Some months that combine extreme precipitation with relatively few landslides (March 2007, July 2007, and February 2013) might be explained by underreporting during the first year of the GLC (March 2007 and July 2007) or the dominance of frozen precipitation (March 2007 and February 2013), which has less of an influence on landslide hazard than rainfall. It is harder to explain the outliers for which more than 60 landslides were reported but mean values of Rx1day were less than 40 mm (September 2010, July 2011, and July 2013). It is possible that pre-conditioning of the soil in previous months that had above average rainfall may have contributed to the clustering of landslides during the following months. The nine months with more than 30 reported landslides are all associated with the summer monsoon, as well as above-average daily precipitation intensity

be seen at the bottom right of Fig. 55.9. These three data points represent months in which intense precipitation failed to trigger landslides; or at least, no landslides were reported for these months. Although these six outliers do not fit the relationship, landslides appear to be associated with increases in Rx1day at the monthly scale, assuming a minimal level of precipitation has occurred.

In general, the mean monthly Rx1day values estimated by FLOR across the study area show a clear linkage between the number of landslides and increasing rainfall estimates. However, there are approximately six months that do not seem to fit this relationship, which we examine in Fig. 55.10. In the three cases where more than 60 landslides were reported, the monthly mean value obscured the existence of local high-intensity precipitation associated with rainfall-triggered landslides. In the three cases where few landslides were reported, we consider how the rainfall distributions may have impacted this result.

Most landslides recorded in September 2010 are clustered near an area of intense precipitation in Himachal Pradesh and Uttarakhand, where Rx1day reaches a maximum of 138 mm. Elsewhere Rx1day only reached 7 mm; the mean value across the

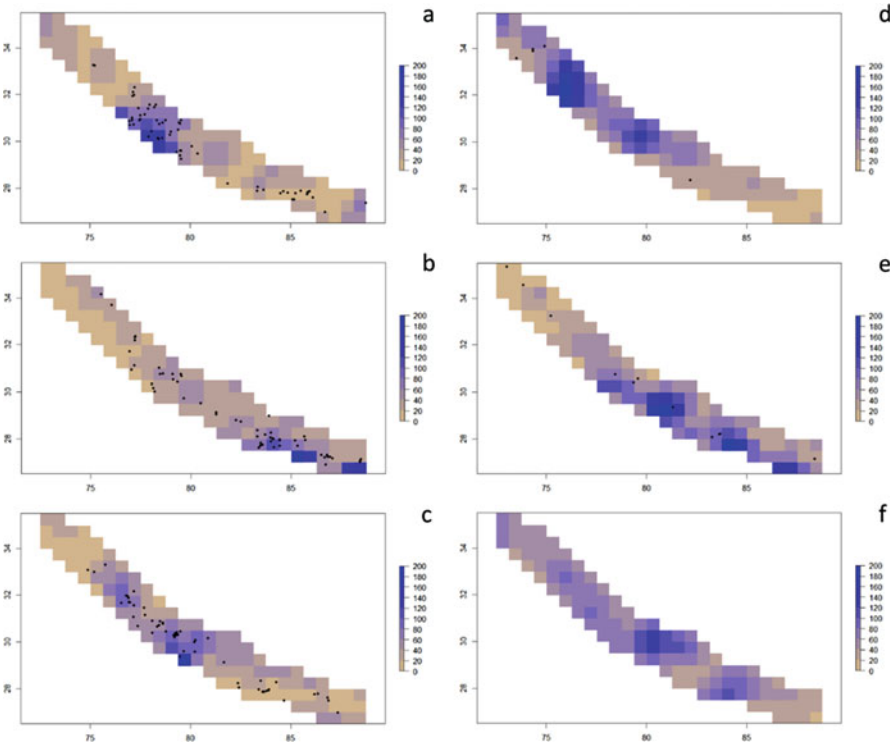

Fig. 55.10 Map of Rx1day monthly estimates (mm) from FLOR and reported landslides across the study region for (**a**) September 2010 (63 landslides), (**b**) July 2011 (62 landslides), (**c**) July 2013 (65 landslides), (**d**) March 2007 (5 landslides), (**e**) July 2007 (11 landslides), and (**f**) February 2013 (0 landslides)

study area was 37 mm. Rx1day for July 2011 ranged from 2 to 166 mm, with a mean of 37. Landslides appear to be clustered in 3 areas: the hills north of Bharatpur and Butwal, Nepal, the hills west of Dhankuta, Nepal, and the mountains of Uttarakhand. A band of extreme precipitation covered the Indian Himalaya and western Nepal in July 2013, with a maximum Rx1day of 167 mm. This appears to be the cause of a loose grouping of reported landslides that occurred from 23–28 July. A second cluster of landslides occurred north of Butwal, Nepal on the 22 July. The timing suggests that both groups of landslides could have been caused by a single meteorological event, but it does not appear to have been modeled by FLOR in the eastern group.

There were also three months that had very few reported landslides but for which Rx1day values were extremely high. Only five landslides were recorded for the month of March 2007, despite the presence of two areas of intense precipitation. Most of the landslides are located along a line between Islamabad, Pakistan, and Srinagar, India. The zones of intense precipitation are located to the southeast, where Rx1day reached a maximum of 187 mm. In this case, the high monthly mean value of Rx1day can be attributed to precipitation in the western half of the study area, but the geographic distribution of landslides leaves the connection between extreme precipitation and slope failure unclear. July 2007 exhibited intense precipitation to much of the study area (peak of 198 mm). In contrast, the western end of the study area experienced no more than 2 mm of precipitation per day, according to FLOR. Despite the clear spatial distribution of extreme precipitation, landslide reporting did not follow this pattern. No landslides were reported for February 2013 despite intense precipitation at multiple locations. Rx1day ranged from 14 to 134 mm. These examples point to the fact that the landslide inventory is highly variable between years and months owing to the availability of reports, time spent by the cataloger, and uncertainty in the timing and location of the GLC reports within this region. The variability may also occur because landslide triggering is a stochastic process with complex failure mechanisms; high rainfall intensity does not guarantee subsequent slope failures.

55.5 Discussion

The extreme precipitation observed within the study area across multiple indices and datasets (Fig. 55.2) suggests that it can be a factor in determining the concentration of landslides at a seasonal scale. Results also show that TMPA and FLOR behave similarly when estimating extreme precipitation indices for both geographic (Fig. 55.2) and seasonal (Figs. 55.5 and 55.7) distributions over the study area. Comparing TMPA and FLOR seasonally highlights several discrepancies, particularly during winter when there is a much more pronounced peak in FLOR relative to TMPA (Fig. 55.5). This may be explained by the presence of frozen precipitation within the winter westerlies that FLOR is able to resolve but is below the sensitivity threshold for TMI's microwave channels onboard the TRMM. Dividing the study area at 80°E reveals that the pre-monsoon landslides were limited to the western side

of the study area (Fig. 55.7). This regional variation was mostly reflected by the monthly distribution of Rx1day calculated from both TMPA and FLOR, which showed higher precipitation intensity in spring and lower precipitation intensity in summer for the western zone. However, the distribution of precipitation is much more equally spread between the two zones than the distribution of landslides. We do not assume a linear response to increases in heavy precipitation; rather, landslides might become much more common after local precipitation exceeds historical maximum accumulations. This pattern also appears in the disaggregated monthly means (Fig. 55.9). Overall, extreme precipitation indices derived from both FLOR and TMPA reflect the seasonal cycle of landslides well.

Trends in extreme precipitation indices across the study region are more variable and less statistically significant (Fig. 55.3), largely due to the short time period for which satellite precipitation data is available. The trends for some frequency-based extreme precipitation indices relate to more common events and may reflect medium-term climate cycles rather than the long-term patterns that could be attributed to global climate change. This points to the opportunity to leverage the longer simulations provided by FLOR to provide a more statistically robust representation of extremes. Work is ongoing to evaluate and apply the longer retrospective record provided by FLOR for improved characterizations of regional precipitation extremes.

The co-occurrence of landslide distribution and extreme indices such as Rx1day suggest that some of the ETCCDI indices (specifically Rx1day and Rx5day) are valuable for characterizing seasonal patterns of landslides regionally. However, the presence of similarly high values just south of the study area suggests that rainfall triggering is not the only factor that modulates this relationship (Fig. 55.11). Landslides tend to be broadly distributed and associated with roads or other

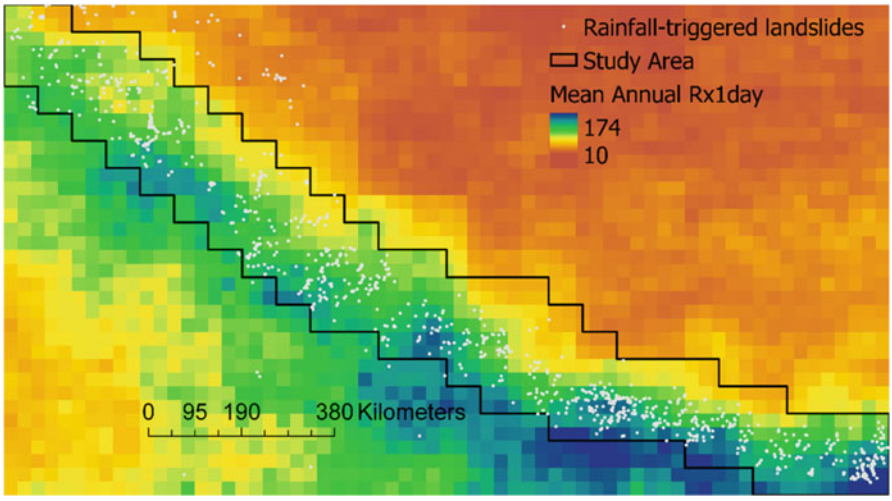

Fig. 55.11 Landslides appear to be slightly more common in grid cells with higher mean values of Rx1day (TMPA shown) and other ETCCDI indices, but the relationship does not appear to be very strong

anthropogenic features, rather than clustered within the rainiest grid cells. Geologic, geometric, and other controls on slope stability must be considered to fully explain the geographic distribution of landslides. Coupling landslide susceptibility maps with the precipitation thresholds or indices can provide both the spatial and temporal characterization of potential landslide activity in near real time (e.g., Kirschbaum and Stanley 2018).

Although the GLC is known to be incomplete (Kirschbaum et al. 2015), no seasonal bias in landslide reporting has been identified. The GLC does not rely on remote sensing, which might be affected by cloud cover or vegetative growth. Although events are entered into the database primarily during the months of June and July, this is unlikely to bias the GLC because the compilation methodology relies on media alerts saved consistently throughout the year. Thus, the monthly distribution is likely to be accurate, even if the annual number of landslides is a gross underestimate. Additionally, we believe the effectiveness of the GLC collection effort has improved over the last decade. In particular, the earliest years are probably underreported relative to later years (Fig. 55.8). If so, the relationship between extreme precipitation indices and annual landslide activity may be much stronger than it appears in Fig. 55.4. Petley (2016) has produced an independent inventory of fatal landslides in Nepal from 1980 to the present with methods similar to the GLC. The year 2008 was the third most active, and a high number of landslides occurred in the years 2007 and 2009 (Petley 2016). The year 2010 has previously been identified as a peak in landslide activity, both in the region (Kirschbaum et al. 2012) and worldwide (Petley 2011; Kirschbaum et al. 2012). The extreme precipitation indices largely corroborate that assessment (Fig. 55.4). Petley (2016) also identified a spike in fatal landslides in 2016, the year after the Gorkha earthquake. However, the GLC does not show a similar increase over the broader study area, and the number of landslides for 2016 appears to be in line with the intensity of extreme precipitation (Fig. 55.4).

The GLC does show a high level of interannual variability, both in annual and monthly totals (Fig. 55.8). Although the first three years of the GLC might not have benefited from advances in Google Alerts and other enhancements of the GLC methodology, we suggest that the variation in subsequent years might be due to a different issue: the nonlinear response of marginally stable slopes to rainfall intensity. Figure 55.9 shows a large number of months with little to no landslide activity. In general, the mean value of Rx1day across the study area is below 15 mm for these months. The remaining months show a positive, but highly variable relationship between increases in extreme precipitation and the number of landslides reported.

We evaluated each of the six months that appeared to defy this relationship. In the three cases where more than 60 landslides were reported, the monthly mean value obscured the existence of regional high-intensity precipitation associated with rainfall-triggered landslides. According to rain-gauge records, heavy precipitation was spread across the state of Uttarakhand, but concentrated on the 18 and 19 September 2010 (Sharma 2012). On the 18th, daily rainfall intensity reached 130, 164, and 458 mm at the Dwarahat, Katarmal, and Nainital meteorological stations, respectively. While the first two are very similar to the modeled precipitation, FLOR did not even approach the latter total. There has been some debate as to whether

natural or anthropogenic factors were more important in preparing the ground for a catastrophe (Sati et al. 2011; Haigh and Rawat 2011), but it is almost certain that extreme rainfall over a large area triggered the disaster. Numerous landslides were reported in locations where FLOR precipitation estimates did not show extreme rainfall, which may be a function of the nudging scheme used to represent rainfall for the individual months (Fig. 55.10) or limitations in GCM performance when representing sub-daily variability (Covey et al. 2018). In addition, anthropogenic impacts, landslides preceding peak rainfall intensities, or incorrectly dated events add uncertainty and further complexity to what event(s) accurately triggered the landslides. The relatively low number of landslides in the months of March and July 2007 could be attributed to subsequent improvements in the GLC methodology, but the absence of rainfall-triggered landslides in February 2013 cannot be as clearly explained. In fact, landslides have been reported for this month, but these are associated with falling snow, not rain. Heavy snowfall usually has a less immediate and profound effect on slope stability than rainfall—unless rain is occurring on top of the snowpack, which may increase potential for runoff and infiltration.

Results here suggest that extreme precipitation indices may serve as a useful proxy for future landslide hazard, but the current comparison provides strong evidence only for the long-term seasonality. Given the nearly global availability of satellite-derived precipitation data, the ETCCDI indices can be calculated globally to determine the spatial distribution of extremes at an annual or decadal scale (Fig. 55.12). The potential applicability as well as the limitations of applying these

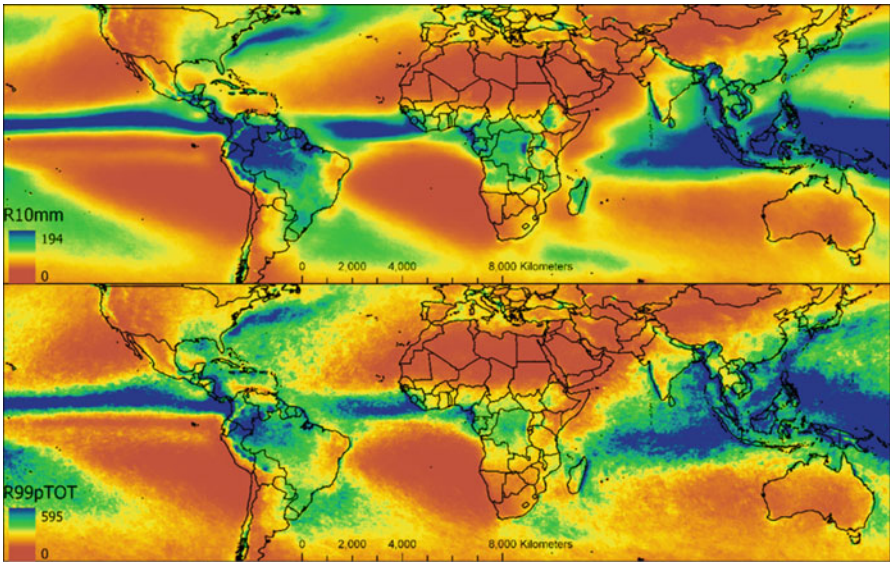

Fig. 55.12 The mean value of R10mm (TMPA) (top) exhibits a smooth spatial distribution due to its emphasis on less extreme precipitation events. In contrast, R99pTOT (TMPA) (bottom) exhibits a noisy spatial pattern, which suggests that the record is too short to contain the most extreme events at every location

indices as a proxy for landslide activity globally are shown in Fig. 55.12, which highlights R10mm and R99pTOT using the full TMPA record. The relative effects of rare and episodic events such as those represented by R99pTOT are clear, while R10mm highlights more consistent patterns globally.

While the focus of this study was on extreme precipitation indices, extreme temperature indices such as number of frost days (FD) and daily minimum temperature (TN_x) might also be linked to landslide activity in HMA. Temperature could affect the phase of the precipitation, which affects landslide triggering: falling snow is less likely to immediately trigger a landslide than falling rain. Melting snow can trigger landslides, especially when combined with simultaneous rainfall. Rising temperatures could affect antecedent conditions even more strongly by melting permafrost that currently enhances rock mass strength, altering the distribution of vegetation and settlement, opening glacial valleys to new mass wasting processes, and forming new lakes in glacier beds (Haeberli et al. 2017). Given that future increases in temperature are more certain than future increases in extreme precipitation (NCVST 2009), modeling the effects of temperature changes to soil moisture, permafrost, snowfields, vegetation, and glaciers on landslide hazard in HMA is a logical direction for future research.

55.6 Conclusions

This work highlights the utility of satellite and GCM precipitation estimates to establish the co-occurrence of extreme precipitation and landslides over the HMA region. While several of the ETCCDI indices demonstrate value in identifying extreme rainfall that could result in landslide activity, incorporation of terrain characteristics is also fundamental to understanding landslide triggering. Furthermore, the distribution of rainfall-triggered landslides within the study area does not appear to be controlled solely by extreme precipitation as measured by mean ETCCDI indices. Antecedent soil moisture and local relief, which may amplify local precipitation maxima through orographic processes, are both critical and were not analyzed in the current work.

Satellite and GCM data agree that the seasonal cycle of rainfall-triggered landslide activity in HMA is captured by the ETCCDI extreme precipitation indices. Even though winter precipitation plays a greater role in the western half of the study area, the landslide cycle is still dominated by the monsoon. This cycle is well known, but it is remarkable that a single number – mean maximum daily precipitation – so thoroughly represents landslide behavior in the study area. The same is unlikely to be true of other regions; in some places, antecedent conditions such as snow cover, vegetative cover, and rainfall may obfuscate the relationship. In cool climates, it will be necessary to treat frozen and liquid precipitation separately, as the effects of snow upon slope stability may be delayed by months. Nevertheless, extreme precipitation indices may be valuable in detecting changes to landslide seasonality in forecasts from global or regional climate models.

The relationship between the annual means of the indices and the annual number of landslides appears to be weak. However, the GLC is not a complete and unbiased record of landslides, nor are alternative datasets, such as remotely sensed inventories or other global landslide inventories (e.g., Froude and Petley 2018). We remain optimistic about the practice of using extreme precipitation indices as a shorthand for landslide hazard under various climate scenarios, but quantification of the relationship will rely on improvements to both the size and comprehensiveness of landslide inventories. Direct modeling of landslides under varying rainfall, soil moisture, and temperature conditions could better explain the historic patterns of landslide activity.

Acknowledgements The authors gratefully acknowledge reviews of this manuscript provided by Robert Emberson (USRA/NASA), Nathaniel Johnson (NOAA), and John Lanzante (NOAA). This work was supported by the NASA High Mountain Asia Project. Specifically, support for D. Kirschbaum and T. Stanley was provided by NASA grant #N5-HMA15-0035. Support for S. Kapnick and S. Pascale was provided by NASA grant #15-HMA15-0016. S. Pascale is also supported by the NOAA CICS grant – NA14OAR4320106.

References

Adler, R. F., Huffman, G. J., Chang, A., Ferraro, R. R., Xie, P., Janowiak, J., Rudolf, B., Schneider, U., Curtis, S., Bolvin, D. T., Gruber, A., Susskind, J., Arkin, P. A., & Nelkin, E. (2003). The version-2 Global Precipitation Climatology Project (GPCP) monthly precipitation analysis (1979–present). *Journal of Hydrometeorology, 4*, 1147–1167. https://doi.org/10.1175/1525-7541(2003)004<1147:TVGPCP>2.0.CO;2.

Ávila, A., Justino, F., Wilson, A., Bromwich, D., & Amorim, M. (2016). Recent precipitation trends, flash floods and landslides in southern Brazil. *Environmental Research Letters, 11*, 114029. https://doi.org/10.1088/1748-9326/11/11/114029.

Barros, A. P., Joshi, M., Putkonen, J., & Burbank, D. W. (2000). A study of the 1999 monsoon rainfall in a mountainous region in Central Nepal using TRMM products and rain gauge observations. *Geophysical Research Letters, 27*, 3683–3686. https://doi.org/10.1029/2000GL011827.

Barros, A. P., Kim, G., Williams, E., & Nesbitt, S. W. (2004). Probing orographic controls in the Himalayas during the monsoon using satellite imagery. *Natural Hazards and Earth System Sciences, 4*, 29–51. https://doi.org/10.5194/nhess-4-29-2004.

Bharti, V., & Singh, C. (2015). Evaluation of error in TRMM 3B42V7 precipitation estimates over the Himalayan region. *Journal of Geophysical Research, 120*, 12,458–12,473. https://doi.org/10.1002/2014JD022121.

Bronaugh, D. (2015). Climdex.pcic: PCIC Implementation of Climdex Routines. Available at https://rdrr.io/cran/climdex.pcic/, last accessed 2 Dec 2018.

Cepeda, J., Hoeg, K., & Nadim, F. (2010). Landslide-triggering rainfall thresholds: A conceptual framework. *Quarterly Journal of Engineering Geology and Hydrogeology, 43*, 69–84. https://doi.org/10.1144/1470-9236/08-066.

Chen, J. C., Huang, W. S., Jan, C. D., & Yang, Y. H. (2012). Recent changes in the number of rainfall events related to debris-flow occurrence in the Chenyulan Stream Watershed, Taiwan. *Natural Hazards and Earth System Sciences, 12*, 1539–1549. https://doi.org/10.5194/nhess-12-1539-2012.

Covey, C., Doutriaux, C., Gleckler, P. J., & Taylor, K. E. (2018). High-frequency intermittency in observed and model-simulated precipitation. *Geophysical Research Letters, 45*, 1–9. https://doi.org/10.1029/2018GL078926.

Dahal, R. K., & Hasegawa, S. (2008). Representative rainfall thresholds for landslides in the Nepal Himalaya. *Geomorphology, 100*, 429–443. https://doi.org/10.1016/j.geomorph.2008.01.014.

Delworth, T. L., & Zeng, F. (2014). Regional rainfall decline in Australia attributed to anthropogenic greenhouse gases and ozone levels. *Nature Geoscience, 7*, 583–587. https://doi.org/10.1038/ngeo2201.

Delworth, T. L., Rosati, A., Anderson, W., Adcroft, A. J., Balaji, V., Benson, R., Dixon, K., Griffies, S. M., Lee, H.-C., Pacanowski, R. C., Vecchi, G. A., Wittenberg, A. T., Zeng, F., & Zhang, R. (2011). Simulated climate and climate change in the GFDL CM2.5 High-Resolution Coupled Climate Model. *Journal of Climate, 25*, 2755–2781. https://doi.org/10.1175/JCLI-D-11-00316.1.

Delworth, T. L., Zeng, F., Vecchi, G. A., Yang, X., Zhang, L., & Zhang, R. (2016). The North Atlantic Oscillation as a driver of rapid climate change in the Northern Hemisphere. *Nature Geoscience, 9*, 509–512. https://doi.org/10.1038/ngeo2738.

Froude, M. J., & Petley, D. N. (2018). Global fatal landslide occurrence from 2004 to 2016. *Natural Hazards and Earth System Sciences, 18*, 2161–2181. https://doi.org/10.5194/nhess-18-2161-2018.

Gabet, E. J., Burbank, D. W., Putkonen, J. K., Pratt-Sitaula, B. A., & Ojha, T. (2004). Rainfall thresholds for landsliding in the Himalayas of Nepal. *Geomorphology, 63*, 131–143. https://doi.org/10.1016/j.geomorph.2004.03.011.

Haeberli, W., Schaub, Y., & Huggel, C. (2017). Increasing risks related to landslides from degrading permafrost into new lakes in de-glaciating mountain ranges. *Geomorphology, 293*, 405–417. https://doi.org/10.1016/J.GEOMORPH.2016.02.009.

Haigh, M., & Rawat, J. S. (2011). Landslide causes: Human impacts on a Himalayan landslide swarm. *Belgeo, 3*(3–4), 201–220. https://doi.org/10.4000/belgeo.6311.

Hijmans, R. J. (2015). Raster: Geographic Data Analysis and Modeling. R package version 2.4-15. Available at https://cran.r-project.org/web/packages/raster/index.html, last accessed 2 Dec 2018.

Huffman, G. J., Adler, R. F., Bolvin, D. T., & Nelkin, E. J. (2010). The TRMM multi-satellite precipitation analysis (TMPA). In F. Hossain & M. Gebremichael (Eds.), *Satellite rainfall applications for surface hydrology* (pp. 3–22). Dordrecht: Springer. https://doi.org/10.1007/978-90-481-2915-7_1.

Ines, A. V. M., & Hansen, J. W. (2006). Bias correction of daily GCM rainfall for crop simulation studies. *Agricultural and Forest Meteorology, 138*, 44–53. https://doi.org/10.1016/j.agrformet.2006.03.009.

Kapnick, S. B., Delworth, T. L., Ashfaq, M., Malyshev, S., & Milly, P. C. D. (2014). Snowfall less sensitive to warming in Karakoram than in Himalayas due to a unique seasonal cycle. *Nature Geoscience, 7*, 834–840. https://doi.org/10.1038/ngeo2269.

Karki, R., Hasson, S., Schickhoff, U., & Scholten, T. (2017). Rising precipitation extremes across Nepal. *Climate, 5*, 1–26. https://doi.org/10.3390/cli5010004.

Kendall, M. G. (1948). *Rank correlation methods* (p. 272). Oxford: Oxford University Press. ISBN: 0195208374.

Kirschbaum, D. B., & Stanley, T. (2018). Satellite-based assessment of rainfall-triggered landslide hazard for situational awareness. *Earth's Future, 6*, 505–523. https://doi.org/10.1002/2017EF000715.

Kirschbaum, D. B., Adler, R. F., Hong, Y., Hill, S., & Lerner-Lam, A. (2010). A global landslide catalog for hazard applications: Method, results, and limitations. *Natural Hazards, 52*, 561–575. https://doi.org/10.1007/s11069-009-9401-4.

Kirschbaum, D. B., Adler, R. F., Adler, D., Peters-Lidard, C., & Huffman, G. J. (2012). Global distribution of extreme precipitation and high-impact landslides in 2010 relative to previous years. *Journal of Hydrometeorology, 13*, 1536–1551. https://doi.org/10.1175/JHM-D-12-02.1.

Kirschbaum, D. B., Stanley, T., & Zhou, Y. (2015). Spatial and temporal analysis of a Global Landslide Catalog. *Geomorphology, 249*, 4–15. https://doi.org/10.1016/j.geomorph.2015.03.016.

Mann, H. B. (1945). Nonparametric tests against trend. *Econometrica, 13*, 245. https://doi.org/10.2307/1907187.

Nadim, F., Kjekstad, O., Peduzzi, P., Herold, C., & Jaedicke, C. (2006). Global landslide and avalanche hotspots. *Landslides, 3*, 159–173. https://doi.org/10.1007/s10346-006-0036-1.

NCVST. (2009). Vulnerability through the eyes of vulnerable: Climate change induced uncertainties and Nepal's development predicaments. Boulder, CO. Available at https://www.preventionweb.net/publications/view/12565, last accessed 2 Dec 2018.

Panday, P. K., Thibeault, J., & Frey, K. E. (2015). Changing temperature and precipitation extremes in the Hindu Kush-Himalayan region: An analysis of CMIP3 and CMIP5 simulations and projections. *International Journal of Climatology, 35*, 3058–3077. https://doi.org/10.1002/joc.4192.

Pascale, S., Boos, W. R., Bordoni, S., Delworth, T. L., Kapnick, S. B., Murakami, H., Vecchi, G. A., & Zhang, W. (2017). Weakening of the North American monsoon with global warming. *Nature Climate Change, 7*, 806–812. https://doi.org/10.1038/nclimate3412.

Petley, D. N. (2011). Global deaths from landslides in 2010 (updated to include a comparison with previous years). *Landslide Blog*. Available at https://blogs.agu.org/landslideblog/2011/02/05/global-deaths-from-landslides-in-2010/, last accessed 2 Dec 2018.

Petley, D. N. (2012). Global patterns of loss of life from landslides. *Geology, 40*, 927–930. https://doi.org/10.1130/G33217.1.

Petley, D. N. (2016). Nepal landslides 2016: Losses at the end of the rainy season – The Landslide Blog – AGU Blogosphere. Available at https://blogs.agu.org/landslideblog/2016/08/01/2016-landslide-losses/, last accessed 2 Dec 2018.

Petley, D. N., Hearn, G. J., Hart, A., Rosser, N. J., Dunning, S. A., Oven, K., & Mitchell, W. A. (2007). Trends in landslide occurrence in Nepal. *Natural Hazards, 43*, 23–44. https://doi.org/10.1007/s11069-006-9100-3.

Pohlert, T. (2017). Tend: Non-Parametric Trend Tests and Change-Point Detection. Available at https://rdrr.io/cran/trend/, last accessed 2 Dec 2018.

R Core Team (2013) R: A language and environment for statistical computing. *R Foundation for Statistical Computing*. Available at http://www.r-project.org/, last accessed 2 Dec 2018.

Revolution Analytics, and S. Weston. (2015) Foreach: Provides Foreach Looping Construct for R. Available at https://rdrr.io/rforge/foreach/, last accessed 2 Dec 2018.

Sati, S. P., Sundriyal, Y. P., Rana, N., & Dangwal, S. (2011). Recent landslides in Uttarakhand: Nature's fury or human folly. *Current Science, 100*, 1617–1620. Available at https://www.researchgate.net/publication/285718177_Recent_landslides_in_Uttarakhand_Nature%27s_fury_or_human_folly, last accessed 2 Dec 2018.

Sen, P. K. (1968). Estimates of the regression coefficient based on Kendall's Tau. *Journal of the American Statistical Association, 63*, 1379–1389. https://doi.org/10.1080/01621459.1968.10480934.

Sharma, S. (2012). Catastrophic hydrological event of 18 and 19 September 2010 in Uttarakhand, Indian Central Himalaya – An analysis of rainfall and slope failure. *Current Science, 102*, 327–332. Available at https://www.researchgate.net/publication/224960685_Catastrophic_hydrological_event_of_18_and_19_September_2010_in_Uttarakhand_Indian_Central_Himalaya_-_an_analysis_of_rainfall_and_slope_failure, last accessed 2 Dec 2018.

Theil, H. (1992). A rank-invariant method of linear and polynomial regression analysis. In B. Raj & J. Koerts (Eds.), *Henri Theil's Contributions to Economics and Econometrics* (Advanced Studies in Theoretical and Applied Econometrics, 23). Dordrecht: Springer. https://doi.org/10.1007/978-94-011-2546-8_20.

Vecchi, G. A., Delworth, T., Gudgel, R., Kapnick, S., Rosati, A., Wittenberg, A. T., Zeng, F., Anderson, W., Balaji, V., Dixon, K., Jia, L., Kim, H.-S., Krishnamurthy, L., Msadek, R., Stern, W. F., Underwood, S. D., Villarini, G., Yang, X., & Zhang, S. (2014). On the seasonal forecasting of regional tropical cyclone activity. *Journal of Climate, 27*, 7994–8016. https://doi.org/10.1175/JCLI-D-14-00158.1.

World Climate Research Programme. (2018). About ETCCDI. Available at https://www.wcrp-climate.org/etccdi, last accessed 2 Dec 2018.

Yang, M., Chen, X., & Cheng, C. S. (2016). Hydrological impacts of precipitation extremes in the Huaihe River Basin, China. *Springerplus, 6*, 1731. https://doi.org/10.1186/s40064-016-3429-1.

Yang, X., Jia, L., Kapnick, S. B., Delworth, T. L., Vecchi, G. A., Gudgel, R., Underwood, S., & Zeng, F. (2018). On the seasonal prediction of the western United States El Niño precipitation pattern during the 2015/16 winter. *Climate Dynamics, 51*, 3765–3783. https://doi.org/10.1007/s00382-018-4109-3.

Zhang, W., Vecchi, G. A., Murakami, H., Delworth, T., Wittenberg, A. T., Rosati, A., Underwood, S., Anderson, W., Harris, L., Gudgel, R., Lin, S.-J., Villarini, G., & Chen, J.-H. (2015). Improved simulation of tropical cyclone responses to ENSO in the Western North Pacific in the High-Resolution GFDL HiFLOR Coupled Climate Model. *Journal of Climate, 29*, 1391–1415. https://doi.org/10.1175/JCLI-D-15-0475.1.